

Near-Infrared-Plasmonic Energy Upconversion in a Nonmetallic Heterostructure for Efficient H₂ Evolution from Ammonia Borane

Zhenyi Zhang, Yang Liu, Yurui Fang, Baosheng Cao, Jindou Huang, Kuichao Liu, and Bin Dong*

Plasmonic metal nanostructures have been widely used to enhance the upconversion efficiency of the near-infrared (NIR) photons into the visible region via the localized surface plasmon resonance (LSPR) effect. However, the direct utilization of low-cost nonmetallic semiconductors to both concentrate and transfer the NIR-plasmonic energy in the upconversion system remains a significant challenge. Here, a fascinating process of NIR-plasmonic energy upconversion in Yb³⁺/Er³⁺-doped NaYF₄ nanoparticles (NaYF₄:Yb-Er NPs)/W₁₈O₄₉ nanowires (NWs) heterostructures, which can selectively enhance the upconversion luminescence by two orders of magnitude, is demonstrated. Combined with theoretical calculations, it is proposed that the NIR-excited LSPR of W₁₈O₄₉ NWs is the primary reason for the enhanced upconversion luminescence of NaYF₄:Yb-Er NPs. Meanwhile, this plasmon-enhanced upconversion luminescence can be partly absorbed by the W₁₈O₄₉ NWs to re-excite its higher energy LSPR, thus leading to the selective enhancement of upconversion luminescence for the NaYF₄:Yb-Er/W₁₈O₄₉ heterostructures. More importantly, based on this process of plasmonic energy transfer, an NIR-driven catalyst of NaYF₄:Yb-Er NPs@W₁₈O₄₉ NWs quasi-core/shell heterostructure, which exhibits a ≈35-fold increase in the catalytic H₂ evolution from ammonia borane (BH₃NH₃) is designed and synthesized. This work provides insight on the development of nonmetallic plasmon-sensitized optical materials that can potentially be applied in photocatalysis, optoelectronic, and photovoltaic devices.

their unique capability to concentrate and amplify the incident light intensity near the surface of plasmonic nanostructures.^[1–3] As a classic plasmonic “optical antenna,” noble metal nanostructures with tunable LSPR energy are frequently introduced into nanomaterials to promote their performance in light absorption and/or emission via plasmonic energy transfer from noble metal to neighboring optical nanomaterials.^[4–6] For example, coupling appropriate nanostructures of plasmonic Au or Ag with upconversion nanomaterials, in particular trivalent lanthanide ions (Ln³⁺)-doped NaYF₄ nanoparticles (NPs), can achieve enhanced upconversion luminescence in the visible light region by converting lower frequency incident photons at 980 nm with high effectivity.^[7–9] This paradigm has been regarded as a promising tactic to use the low-energy NIR light, which makes up almost half of the solar energy (≈40%), in the field of solar-to-fuels energy conversion.^[10,11] From a plasmonic point of view, the overlapping spectra between LSPR bands of noble metals and the excitation/emission bands of upconversion NPs

Over the past several decades, the fascinating photophysical phenomena of localized surface plasmon resonance (LSPR) have attracted significant interests in research areas such as electronics, photonics, and catalysis. This is mainly due to

would result in a highly efficient upconversion of NIR to visible light.^[12,13] Although some specific metallic structures, such as long nanowires (NWs) and nanoforest, can easily provide a very wide band for simultaneously matching the excitation

Prof. Z. Zhang, Y. Liu, Prof. B. Cao, J. Huang, K. Liu, Prof. B. Dong
Key Laboratory of New Energy and Rare Earth Resource Utilization
of State Ethnic Affairs Commission
Key Laboratory of Photosensitive Materials & Devices
of Liaoning Province
School of Physics and Materials Engineering
Dalian Minzu University
18 Liaoh West Road, Dalian 116600, P. R. China
E-mail: dong@dlmu.edu.cn

© 2018 The Authors. Published by WILEY-VCH Verlag GmbH & Co. KGaA, Weinheim. This is an open access article under the terms of the Creative Commons Attribution License, which permits use, distribution and reproduction in any medium, provided the original work is properly cited.

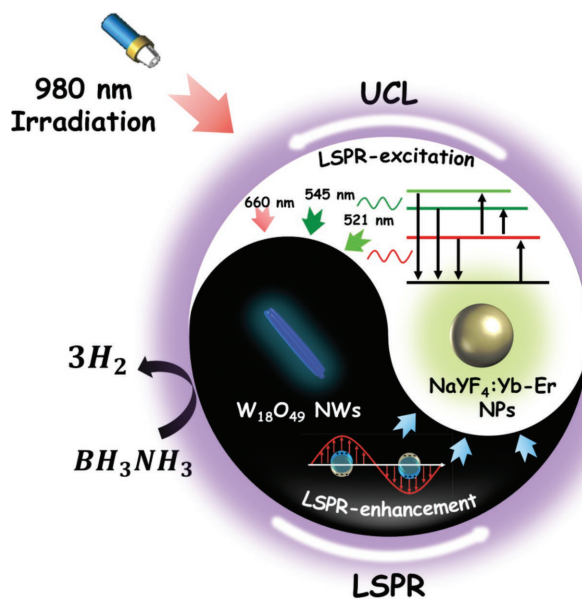
DOI: 10.1002/adv.201800748

Y. Liu
School of Materials Science and Engineering
Dalian University of Technology
Dalian 116024, P. R. China
Prof. Y. Fang
Key Laboratory of Materials Modification by Laser
Electron, and Ion Beams (Ministry of Education)
School of Physics
Dalian University of Technology
Dalian 116024, P. R. China

and emission bands of Ln^{3+} -doped NaYF_4 NPs, manipulating the shapes and sizes of these metallic structures often requires a very complex synthesis process.^[14,15] Furthermore, using noble metals inevitably suffers from high cost and earth rarity. Therefore, exploiting noble-metal-free tractable plasmonic nanostructures to sensitize the upconversion luminescence of Ln^{3+} -doped NaYF_4 NPs is of great significance for boosting the development of NIR-driven energy generation.

Recently, some researches have reported that the LSPR phenomena can also occur on various nonmetal nanostructures of heavily doped nonstoichiometric semiconductors, such as Cu_{2-x}S , Sn-doped In_2O_3 , WO_{3-x} , and MoO_{3-x} .^[16–20] LSPR band and intensity of the semiconductor can be easily controlled via adjusting the stoichiometric ratios, vacancy, or dopant concentrations, as well as phase structures.^[21–23] Among the plasmonic semiconductor nanostructures, tungsten oxide NWs, $\text{W}_{18}\text{O}_{49}$, made via a facile solvothermal method, possess intense LSPR band across the visible and NIR regions due to abundant oxygen vacancies on their surface.^[24–26] Such a broad plasmonic absorption of $\text{W}_{18}\text{O}_{49}$ NWs covers both excitation and emission spectra of $\text{Yb}^{3+}/\text{Er}^{3+}$ -doped NaYF_4 ($\text{NaYF}_4\text{:Yb-Er}$) NPs, which offers an unique opportunity to gain deeper understanding on the influence of the LSPR on the photon absorption and emission processes of the upconversion NPs within the same plasmonic nanostructure. Moreover, plasmonic $\text{W}_{18}\text{O}_{49}$ NWs have demonstrated outstanding catalytic performance for the H_2 evolution from ammonia borane (BH_3NH_3).^[27] Combining plasmonic $\text{W}_{18}\text{O}_{49}$ NWs with $\text{NaYF}_4\text{:Yb-Er}$ NPs to form a hierarchical heterostructure would also promote the catalytic activity for H_2 evolution due to the LSPR-induced interaction between both nanomaterials. This may reveal a new way to explore the NIR-active catalyst for potential applications for the development of sustainable energy sources.

For the first time, we demonstrate the nonmetallic plasmon-induced selective enhancement of upconversion luminescence in a layer-structured film consisting of $\text{NaYF}_4\text{:Yb-Er}$ NPs as the upconversion layer and $\text{W}_{18}\text{O}_{49}$ NWs as the plasmonic layer. Compared with the individual $\text{NaYF}_4\text{:Yb-Er}$ film, the $\text{NaYF}_4\text{:Yb-Er}/\text{W}_{18}\text{O}_{49}$ film exhibited two orders upconversion enhancement on the green emission originating from the $^2\text{H}_{11/2}-^4\text{I}_{15/2}$ transition of Er^{3+} ions, but a decreased effect from red emission, which was ascribed to Er^{3+} ions with the $^4\text{F}_{9/2}-^4\text{I}_{15/2}$ transition. Combined with the theoretical calculations, we propose that this selective enhancement of upconversion luminescence is caused via LSPR-induced NIR-plasmonic energy upconversion. In this process, $\text{W}_{18}\text{O}_{49}$ NWs convert the NIR energy of incident photons into LSPR oscillation energy that subsequently transfers to the adjacent $\text{NaYF}_4\text{:Yb-Er}$ NPs, thus substantially enhancing the upconversion luminescence intensity based on the plasmon-enhanced localized electric fields and the photothermally improved electron population. The enhanced upconversion luminescence of $\text{NaYF}_4\text{:Yb-Er}$ NPs would then re-excite the LSPR oscillations of $\text{W}_{18}\text{O}_{49}$ NWs in the visible region, resulting in the selective absorption of upconversion luminescence depending on the LSPR band of $\text{W}_{18}\text{O}_{49}$ NWs (Scheme 1). Due to this unique plasmonic energy upconversion phenomenon, an enhanced catalytic activity for H_2 evolution from BH_3NH_3 was achieved over the $\text{NaYF}_4\text{:Yb-Er}$



Scheme 1. Schematic diagram of plasmonic energy upconversion in the $\text{NaYF}_4\text{:Yb-Er}$ NPs/ $\text{W}_{18}\text{O}_{49}$ NWs system upon irradiation at 980 nm.

NPs@ $\text{W}_{18}\text{O}_{49}$ NWs quasi-core/shell structure synthesized via facile solvothermal method.

To clarify the influence of $\text{W}_{18}\text{O}_{49}$ LSPR on the upconversion behavior of $\text{NaYF}_4\text{:Yb-Er}$ NPs, a binary film with layer-on-layer heterostructure was designed and constructed hierarchically onto F-doped SnO_2 (FTO) glass. The FTO glass is chosen as the film substrate, because it contains abundant active sites for benefiting the uniform growth of plasmonic $\text{W}_{18}\text{O}_{49}$ NWs on its surface. Figure 1a shows the schematic illustration of the two-step assembly route and the profile of the $\text{NaYF}_4\text{:Yb-Er}/\text{W}_{18}\text{O}_{49}$ film. During the first step, $\text{W}_{18}\text{O}_{49}$ NWs were grown onto the FTO glass to achieve the plasmonic layer via a solvothermal process; for the second step, the $\text{NaYF}_4\text{:Yb-Er}$ NPs were self-assembled on the top surface of the $\text{W}_{18}\text{O}_{49}$ NWs layer through a solvent evaporation process, therefore forming a thin upconversion-luminescence layer above the plasmonic layer. Meanwhile, two control samples were constructed on the FTO glass: one is the $\text{NaYF}_4\text{:Yb-Er}$ film, which was fabricated by direct self-assembly of $\text{NaYF}_4\text{:Yb-Er}$ NPs onto the FTO glass; the other is the $\text{NaYF}_4\text{:Yb-Er}/\text{N-W}_{18}\text{O}_{49}$ film, where the N- $\text{W}_{18}\text{O}_{49}$ NWs, denoting non-plasmonic $\text{W}_{18}\text{O}_{49}$ NWs, were obtained through the H_2O_2 treatment of plasmonic $\text{W}_{18}\text{O}_{49}$ NWs to passivate their surface oxygen vacancies.

The X-ray diffraction (XRD) pattern of the $\text{NaYF}_4\text{:Yb-Er}/\text{W}_{18}\text{O}_{49}$ film shows three sets of characteristic peaks, belonging to hexagonal $\beta\text{-NaYF}_4$, monoclinic $\text{W}_{18}\text{O}_{49}$, and tetragonal SnO_2 , respectively (Figure 1b). Scanning electron microscopic (SEM) images display both top surface (Figure 1c) and cross section (Figure 1d) of the above film. It can be seen that $\text{NaYF}_4\text{:Yb-Er}$ NPs with a mean size of ≈ 40 nm are interconnected and cover the top surface of the composite film, thus forming a thin upconversion-luminescence layer. Furthermore, $\text{W}_{18}\text{O}_{49}$ NWs with diameters of 20–40 nm and lengths of 0.5–1.0 μm aligned in random orientations on the FTO glass, where they interweaved to compose a plasmonic layer (of ≈ 500 nm

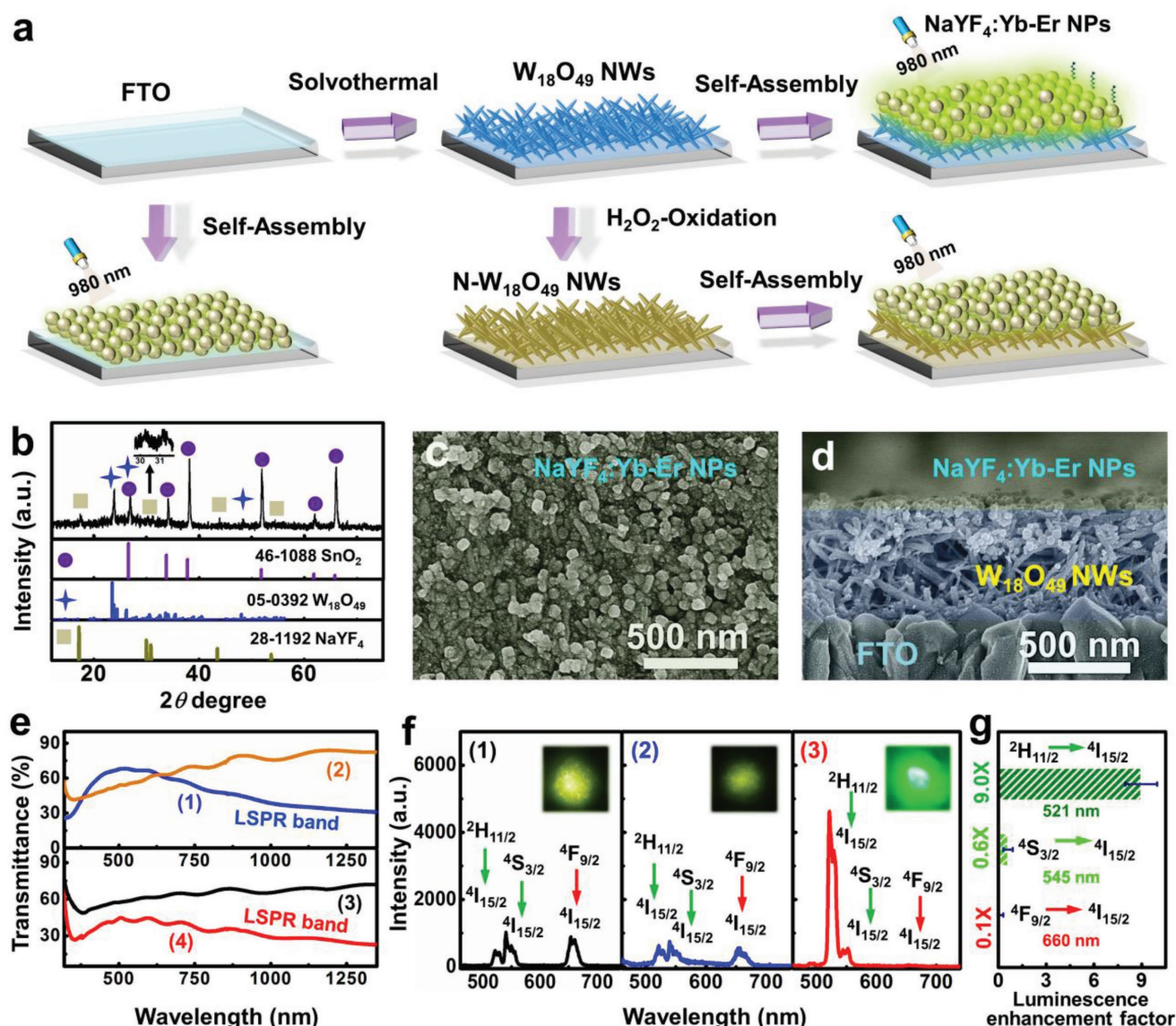


Figure 1. a) Fabrication processes of the NaYF₄:Yb-Er, NaYF₄:Yb-Er/ $W_{18}O_{49}$, and NaYF₄:Yb-Er/N- $W_{18}O_{49}$ films on FTO glass. b) XRD pattern of the as-fabricated NaYF₄:Yb-Er/ $W_{18}O_{49}$ film. SEM images of c) the top view and d) the side view of the NaYF₄:Yb-Er/ $W_{18}O_{49}$ film. e) Transmittance spectra of 1) $W_{18}O_{49}$ NWs, 2) N- $W_{18}O_{49}$ NWs, 3) NaYF₄:Yb-Er/N- $W_{18}O_{49}$, and 4) NaYF₄:Yb-Er/ $W_{18}O_{49}$ films. The insets provide the corresponding micro-area optical images achieved under irradiation at 980 nm. g) Histogram of enhancement factors calculated via the luminescence intensity ratios of NaYF₄:Yb-Er/ $W_{18}O_{49}$ film to the NaYF₄:Yb-Er film at the different emission wavelengths.

thickness) below the upconversion-luminescence layer. The randomly tilted growth of $W_{18}O_{49}$ NWs on the film enabled the majority of self-assembled NaYF₄:Yb-Er NPs to directly contact the side surface of plasmonic $W_{18}O_{49}$ NWs. The control sample of NaYF₄:Yb-Er/N- $W_{18}O_{49}$ film was identical to the NaYF₄:Yb-Er/ $W_{18}O_{49}$ film in structural features and component morphology. Furthermore, the NaYF₄:Yb-Er film possessed similar thickness as the upconversion luminescence layer in the NaYF₄:Yb-Er/ $W_{18}O_{49}$ film (Figure S1, Supporting Information). Figure 1e presents the comparison transmittance spectra of the plasmonic $W_{18}O_{49}$ -based film and the N- $W_{18}O_{49}$ -based film on the FTO glass. The plasmonic $W_{18}O_{49}$ NWs grown on the FTO glass exhibited a low transmittance in the visible–NIR

region. Meanwhile, the transmittance is dependent on the incident wavelength. These observations are in accordance with the intrinsic optical property of $W_{18}O_{49}$ reported in the literatures,^[25–27] confirming that the low transmittance of $W_{18}O_{49}$ -based film is originated from intense LSPR absorption of the $W_{18}O_{49}$ NWs. The LSPR of $W_{18}O_{49}$ NWs could remain at least three months at room temperature and atmosphere pressure (Figure S1, Supporting Information), even though this property derives from the oxygen vacancies. After treatment with H_2O_2 to form N- $W_{18}O_{49}$ NWs, the LSPR absorption disappeared. Importantly, when loading a thin layer of NaYF₄:Yb-Er NPs on the layer of plasmonic $W_{18}O_{49}$ NWs, a distinct LSPR band can still be observed on the spectra of the NaYF₄:Yb-Er/ $W_{18}O_{49}$

film. However, the NaYF₄:Yb-Er/N-W₁₈O₄₉ film did not show the plasmonic absorption band in the visible–NIR region even though it shared the same component morphology with the NaYF₄:Yb-Er/W₁₈O₄₉ film.

Upconversion-luminescence properties of the as-fabricated films were tested via an inverted microscope coupled with a spectrometer and a 980 nm laser diode (Scheme S2, Supporting Information). It is clear that two green emission peaks and one red emission peak appearing on the spectrum of the NaYF₄:Yb-Er film (Figure 1f) are attributed to ²H_{11/2} → ⁴I_{15/2}, ⁴S_{3/2} → ⁴I_{15/2}, and ⁴F_{9/2} → ⁴I_{15/2} transitions of Er³⁺ ions, respectively.^[7–9] Also note that the intensity ratio of green-to-red emission (*I*_{green}/*I*_{red}) is only ≈1.4, resulting in an overall green-yellow color output (see inset of Figure 1f). In the case of the NaYF₄:Yb-Er/N-W₁₈O₄₉ film without plasmonic absorption property, the ratio value of *I*_{green}/*I*_{red} is ≈1.7, with the emission peak profiles almost identical to the corresponding parameters within the NaYF₄:Yb-Er only film. This implies that the upconversion behavior of NaYF₄:Yb-Er NPs is not influenced by the N-W₁₈O₄₉ NWs layer in the composite film. To our surprise, when these N-W₁₈O₄₉ NWs are replaced with the plasmonic W₁₈O₄₉ NWs in the composite film, the NaYF₄:Yb-Er/W₁₈O₄₉ film exhibits a remarkable enhancement in the intensity for green emission;

in particular, the emission peak at 521 nm was nearly one order of magnitude (9.0×) higher than the corresponding emission intensity of the NaYF₄:Yb-Er film (Figure 1g). However, the red emission at 660 nm decreased to 10% of the NaYF₄:Yb-Er film. As a result, the *I*_{green}/*I*_{red} value of NaYF₄:Yb-Er NPs increased to ≈75 after introducing the plasmonic W₁₈O₄₉ NWs layer into the composite film. Thus, a bright green emission became noticeable on the micro-area photograph of the NaYF₄:Yb-Er/W₁₈O₄₉ film in response to excitation with 980 nm (see inset of Figure 1f). It is apparent that a selective enhancement of green upconversion emission was found on the NaYF₄:Yb-Er/W₁₈O₄₉ film.

When the NaYF₄:Yb-Er NPs were deposited on the plasmonic W₁₈O₄₉ NW surface in the composite film, a strong interaction between LSPR and upconversion optical field occurred at their interface since the LSPR band of W₁₈O₄₉ NWs overlapped with both the excitation and emission electric fields of NaYF₄:Yb-Er NPs (see Figure 1e). Upon 980 nm excitation, the W₁₈O₄₉ NWs serve as the “plasmonic antenna” to locally concentrate the NIR energy near the NWs, and then resonantly transfer this energy to adjoining NaYF₄:Yb-Er NPs (Figure 2a).^[28,29] Therefore, the NaYF₄:Yb-Er NPs near the NaYF₄:Yb-Er/W₁₈O₄₉ interface would experience a far more intense excitation electric field based on the surface enhancement effect, which could promote electron

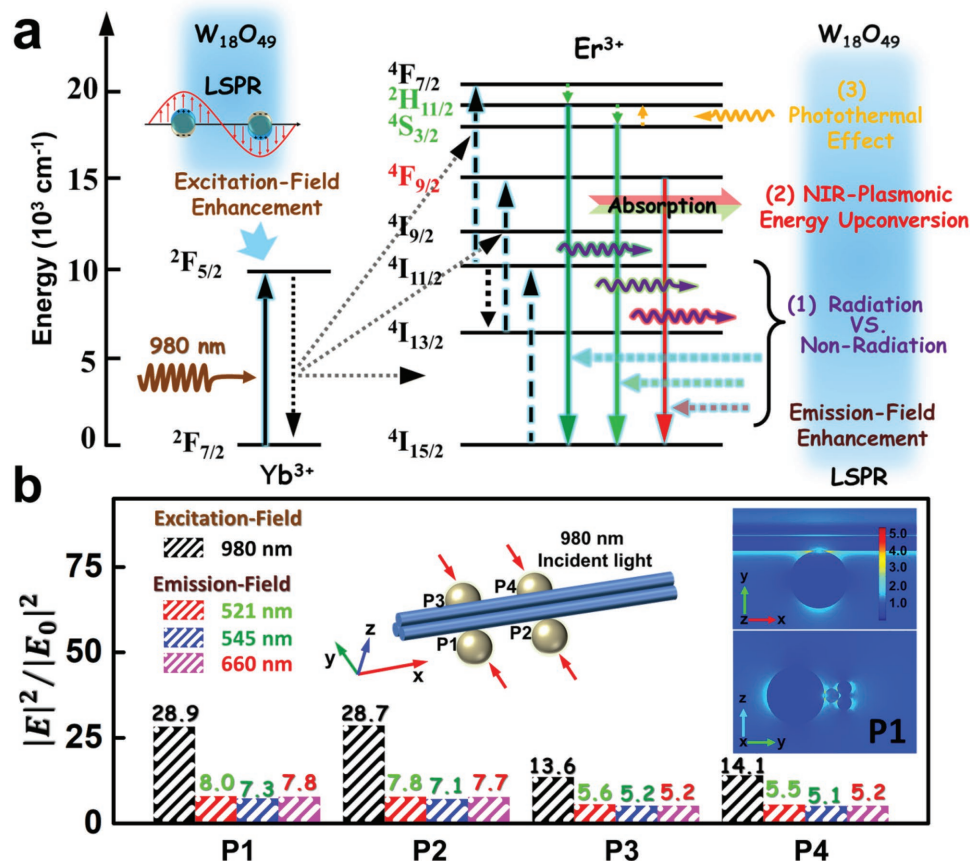


Figure 2. a) Schematic diagram of the interaction between the LSPR effect of W₁₈O₄₉ NWs and the energy-transfer upconversion process of NaYF₄:Yb-Er NPs. b) Simulated enhancements of excitation (980 nm) and emission electric-field intensities (521, 545, and 660 nm) at the plasmonic “hot spots” as a function of the contact positions between the NaYF₄ NPs and W₁₈O₄₉ NWs. Insets show the simulation model of the NaYF₄/W₁₈O₄₉ heterostructure with the NaYF₄ NPs loaded on the representative positions of the W₁₈O₄₉ NWs surface; and the simulation of excitation electric field distribution at position P1 with input irradiation along the y-axis.

population on the excited-state energy levels of Er^{3+} ions, thus resulting in an enhanced upconversion luminescence.^[4,7,30] Meanwhile, the LSPR-enhanced localized electric field can interact with the emission electric field of $\text{NaYF}_4\text{:Yb-Er}$ NPs to boost the radiative decay rate of upconversion process.^[4,7] However, the direct contact of $\text{W}_{18}\text{O}_{49}$ NWs and $\text{NaYF}_4\text{:Yb-Er}$ NPs quenches the upconversion emission to a certain degree due to the nonradiative energy transfer from the $\text{NaYF}_4\text{:Yb-Er}$ NPs (donor) and the adherent $\text{W}_{18}\text{O}_{49}$ NWs (acceptor).^[31–34] Moreover, the upconversion luminescence of $\text{NaYF}_4\text{:Yb-Er}$ NPs can also be absorbed by the adjacent $\text{W}_{18}\text{O}_{49}$ NWs, which selectively weakens the luminescence intensity depending on the absorption band of $\text{W}_{18}\text{O}_{49}$ NWs. Furthermore, the LSPR-induced photothermal effect of $\text{W}_{18}\text{O}_{49}$ NWs can also raise the local temperature of $\text{NaYF}_4\text{:Yb-Er}$ NPs to affect their upconversion process. Based on the above considerations, we proposed that the photophysical mechanism (Figure 2a) for this selective enhancement of upconversion luminescence is attributed to the following three aspects:

- 1) Plasmon-mediated competition between the radiative and nonradiative processes: We employed the finite element method to simulate the localized electric field intensity and distribution near the $\text{NaYF}_4\text{:Yb-Er}$ NPs by plasmon-excitation of $\text{W}_{18}\text{O}_{49}$ NWs. The transmission electron microscopy (TEM) image suggests that the $\text{W}_{18}\text{O}_{49}$ NWs have a bundle-like nanostructure, consisting of several ultrathin secondary NWs with diameters of ≈ 10 nm (Figure S2a, Supporting Information). The TEM image of the $\text{NaYF}_4\text{:Yb-Er}$ NPs confirmed their hexagonal nanostructure with a mean size of ≈ 40 nm (Figure S2b, Supporting Information). To simplify the calculation, a binary heterostructure is proposed in the simulation model, in which the single NaYF_4 NP is selectively loaded on the four representative positions of the bundle-like $\text{W}_{18}\text{O}_{49}$ NWs surface. As illustrated in the inset of Figure 2b, P1 and P2 represent the positions at the quarter and the half of $\text{W}_{18}\text{O}_{49}$ NWs, respectively, which are symmetric to the corresponding sites of P3 and P4. We first simulated the localized electric field distributions of the above four types of $\text{NaYF}_4/\text{W}_{18}\text{O}_{49}$ heterostructures under excitation of 980 nm. When the NaYF_4 NP was tangential to one of the NWs at P1 or P2 on the $\text{W}_{18}\text{O}_{49}$ bundle surface, the maximum electric field intensity enhancement ($|E|^2/|E_0|^2$) could reach ≈ 29 at the plasmonic “hot spots,” i.e., in the vicinity of the $\text{NaYF}_4/\text{W}_{18}\text{O}_{49}$ interface (Figure 2b; Figure S2c, Supporting Information). Furthermore, if the NaYF_4 NP was deposited on either P3 or P4 to tangent simultaneously two of the NWs in the $\text{W}_{18}\text{O}_{49}$ bundle, it can obtain a ≈ 14 -fold increase of the excitation electric field intensity at the $\text{NaYF}_4/\text{W}_{18}\text{O}_{49}$ interface (Figure S2c, Supporting Information). Interestingly, the distal edges of NaYF_4 NPs, opposite from the plasmonic “hot spots,” also showed about a two- to four-fold enhancement of the localized electric field. Also note that the LSPR-enhanced excitation field concentrates mainly on the $\text{NaYF}_4/\text{W}_{18}\text{O}_{49}$ interface with a depth below ≈ 10 nm towards the NaYF_4 . Second, interactions of $\text{W}_{18}\text{O}_{49}$ LSPR with the emission electric field of NaYF_4 NP were assessed through simulating the electric field distributions with emission wavelengths at 521, 545, and 660 nm, respectively (Figures S3–S5, Supporting

Information). The maximum enhancement on the emission electric field intensities of the heterostructures also occurs near the $\text{NaYF}_4/\text{W}_{18}\text{O}_{49}$ interface. Moreover, the enhancement factors at different emission wavelengths fluctuate in a range from 3.4 to 8.0, depending on the contact sites of NaYF_4 NPs on the $\text{W}_{18}\text{O}_{49}$ NWs surface. It should be also noted that the emission electric field enhancement tendency and distributions close to the NaYF_4 NPs almost overlapped with the corresponding features of the excitation electric field enhancement induced by the $\text{W}_{18}\text{O}_{49}$ LSPR. As such, the overall enhancement of optical field at plasmonic “hot spots” of the $\text{NaYF}_4/\text{W}_{18}\text{O}_{49}$ heterostructures ranged from 70 to 220 times (Figure S6, Supporting Information).

However, in our case, the NaYF_4 NPs are directly in contact with the plasmonic $\text{W}_{18}\text{O}_{49}$ NWs and the nonradiative energy transfer to $\text{W}_{18}\text{O}_{49}$ NWs provides an efficient decay channel to quench the upconversion luminescence.^[31–34] The time-resolved luminescence spectroscopy indicated that the lifetimes of $^2\text{I}_{11/2} \rightarrow ^4\text{I}_{15/2}$ (521 nm), $^4\text{S}_{3/2} \rightarrow ^4\text{I}_{15/2}$ (545 nm), and $^4\text{F}_{9/2} \rightarrow ^4\text{I}_{15/2}$ (660 nm) decays for the $\text{NaYF}_4\text{:Yb-Er}/\text{W}_{18}\text{O}_{49}$ film were shorter than the corresponding lifetimes obtained from the individual $\text{NaYF}_4\text{:Yb-Er}$ film (Figure S7, Supporting Information). Combining with the results of selective luminescence enhancement, we confirmed the existence of plasmon-mediated competition between the radiative and nonradiative processes in the $\text{NaYF}_4\text{:Yb-Er}/\text{W}_{18}\text{O}_{49}$ film after 980 nm excitation.^[4,7] The radiative rate enhancement is originated from the plasmon-enhanced emission field, while the nonradiative process in the $\text{NaYF}_4\text{:Yb-Er}/\text{W}_{18}\text{O}_{49}$ film is mainly attributed to the mentioned energy transfer. This nonradiative energy transfer is strongly dependent on the distance between luminescent centers and plasmonic nanostructures.^[33,34] For $\text{NaYF}_4\text{:Yb-Er}$ NPs, the luminescent centers of Er^{3+} ions are uniformly dispersed in the insulating NaYF_4 host.^[30] Thus, the emission quenching process should occur only on the Er^{3+} ions located nearby the $\text{NaYF}_4\text{:Yb-Er}/\text{W}_{18}\text{O}_{49}$ interface. A large number of luminescent centers in the $\text{NaYF}_4\text{:Yb-Er}$ NPs could enjoy the LSPR-enhanced excitation and emission fields with the weakened quenching effect, therefore leading to the enhancement of upconversion luminescence on the $\text{NaYF}_4\text{:Yb-Er}/\text{W}_{18}\text{O}_{49}$ film. To further confirm the existence of nonradiative energy transfer in the $\text{NaYF}_4\text{:Yb-Er}/\text{W}_{18}\text{O}_{49}$ film, we introduced the insulating spacer with different thicknesses to separate the $\text{NaYF}_4\text{:Yb-Er}$ and $\text{W}_{18}\text{O}_{49}$ components, for the purpose of adjusting the energy transfer process (Figure S8, Supporting Information). Interestingly, when the thickness of the insulating spacer is proper, the upconversion luminescence of $\text{NaYF}_4\text{:Yb-Er}$ NPs in the composite film could be further enhanced due to the suppressed nonradiative energy transfer (Figure S8, Supporting Information). Meanwhile, both the green and red emission enhancements were observed on the $\text{NaYF}_4\text{:Yb-Er}/\text{W}_{18}\text{O}_{49}$ film.

To gain a better understanding on the above plasmon-mediated competition process, we established the mathematical model based on a set of rate equations (Figure S9 and Equations (S1)–(S20), Supporting Information). The results demonstrated that the LSPR-enhanced excitation and emission fields were responsible for boosting the upconversion luminescence of

NaYF₄:Yb-Er NPs in the composite film. However, the transfer process of nonradiative energy competed against the LSPR-enhanced emission field to quench the upconversion luminescence. Importantly, we concluded that both the emission field enhancement and the nonradiative energy transfer contributed to the enlargement of intensity ratio between the green and red emissions, leading to a relative strong green emission as compared to the light emission from the NaYF₄:Yb-Er/W₁₈O₄₉ film.

- 2) NIR-plasmonic energy upconversion: The LSPR-enhanced upconversion luminescence of NaYF₄:Yb-Er NPs can be partially absorbed by the adjacent W₁₈O₄₉ NWs due to their spectral overlap, which induces re-excitation of the LSPR effect of W₁₈O₄₉ NWs in the visible region, achieving an NIR-plasmonic energy upconversion process. According to the absorption spectrum of W₁₈O₄₉ NWs, the red emission from the NaYF₄:Yb-Er NPs should be more easily absorbed by the W₁₈O₄₉ NWs as compared to the emitted green light, which leads to a relatively strong green emission of NaYF₄:Yb-Er NPs on the W₁₈O₄₉ NWs film. When the W₁₈O₄₉ NWs layer did not possess the LSPR band in the visible region, both the green and red emission enhancements could be observed on the NaYF₄:Yb-Er/W₁₈O₄₉ film (Figure S9, Supporting Information). Thus, the NIR-plasmonic energy upconversion is one of the reasons for the selective absorption of upconversion luminescence.
- 3) Photothermal effect: After LSPR excitation by 980 nm, the W₁₈O₄₉ NWs can create a super-high temperature surrounding their surfaces (similar to the noble metal nanostructures),^[34,35] which would influence the upconversion luminescence of the neighboring NaYF₄:Yb-Er NPs in the composite film. It is well known that in the case of NaYF₄:Yb-Er, the energy separation ($\approx 840\text{ cm}^{-1}$) between $^2\text{H}_{11/2}$ and $^4\text{S}_{3/2}$ levels can allow the thermally excited population from the $^4\text{S}_{3/2}$ to $^2\text{H}_{11/2}$ level, and a quasi-thermal equilibrium forms between these two levels, resulting in the variation in the transitions of $^2\text{I}_{11/2} \rightarrow ^4\text{I}_{15/2}$ (521 nm) and $^4\text{S}_{3/2} \rightarrow ^4\text{I}_{15/2}$ (545 nm) at an increased temperature (Equation (S21), Supporting Information).^[36–38] As observed in Figure 1f, the NaYF₄:Yb-Er/W₁₈O₄₉ film in our case shows a very large ratio of the green upconversion emissions from the $^2\text{I}_{11/2} \rightarrow ^4\text{I}_{15/2}$ (521 nm) and $^4\text{S}_{3/2} \rightarrow ^4\text{I}_{15/2}$ (545 nm) transitions, which suggests the high

temperature located at the near-surface of NaYF₄:Yb-Er NPs due to the photothermal effect of W₁₈O₄₉ NWs.

Overall, this selective enhancement of upconversion luminescence over the NaYF₄:Yb-Er/W₁₈O₄₉ film was essentially caused by the plasmon-induced energy transfer between the plasmonic W₁₈O₄₉ NWs and NaYF₄:Yb-Er NPs (Figure 2a).

It is worth noting that the LSPR-enhanced near-field effect mainly occurred at the very near region of the NaYF₄/W₁₈O₄₉ interface, which accounts for a small part of the luminescent centers in the NaYF₄ NP. Certainly, if the size of NaYF₄ NP reduces to allow more luminescent centers to locate in the plasmonic field, a more effective enhancement of upconversion luminescence is expected on the NaYF₄/W₁₈O₄₉ film. As we reduced the grain sizes of NaYF₄:Yb-Er NPs in the NaYF₄/W₁₈O₄₉ film, the enhancement factor of upconversion luminescence increased dramatically (Figure 3a; Figure S11, Supporting Information). Grain size reduction ensured that the major part of luminescent centers in the NaYF₄ NP was positioned within the effective interaction distance to enjoy the LSPR-enhanced field, leading to improved enhancement effect on the upconversion luminescence. Further investigation found that the enhancement factors of $^2\text{I}_{11/2} \rightarrow ^4\text{I}_{15/2}$ transitions for all the samples were higher than those of $^4\text{S}_{3/2} \rightarrow ^4\text{I}_{15/2}$ transitions. It reveals that the selective enhancement of upconversion luminescence of NaYF₄ NPs is due to the LSPR of W₁₈O₄₉ NWs in their composite film. Meanwhile, the optimal enhancement factor of 112× was achieved on the $^2\text{I}_{11/2} \rightarrow ^4\text{I}_{15/2}$ transition in 10 nm NaYF₄:Yb-Er NPs (Figure 3a). Although 10 nm NaYF₄:Yb-Er NPs exhibited optimal enhancement effect in our study, 40 nm NaYF₄:Yb-Er NPs showed the largest luminescent intensity after plasmonic sensitization via W₁₈O₄₉ NWs (Figure 3b).

Plasmonic W₁₈O₄₉ NWs are an effective catalyst for boosting the H₂ release from BH₃NH₃ via catalytic hydrolysis.^[21,27,39] Coupling plasmonic W₁₈O₄₉ NWs with Ln³⁺-doped NaYF₄ NPs to construct a hierarchical heterostructure would result in a highly efficient H₂ evolution due to the NIR-plasmonic energy upconversion process. Considering that the catalytic active sites locate on the W₁₈O₄₉ NWs surface, a quasi-core/shell heterostructured catalyst was designed and synthesized via solvothermal growth of W₁₈O₄₉ NWs onto hydrophilic NaYF₄:Yb-Er NPs with a grain

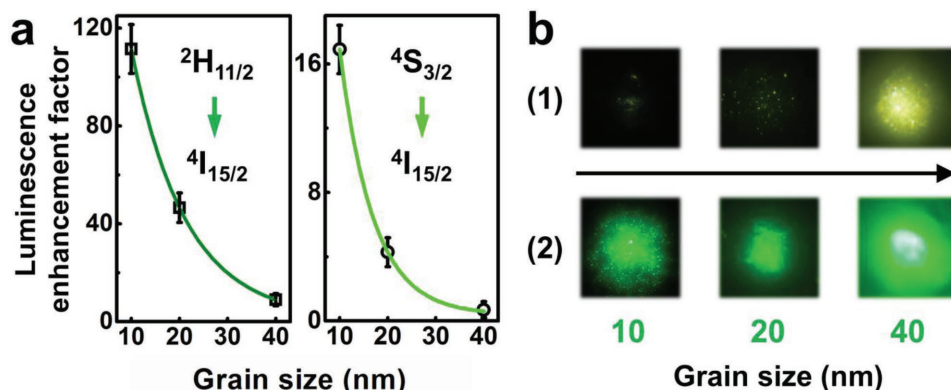


Figure 3. a) Luminescence enhancement factor of $^2\text{H}_{11/2}$ and $^4\text{S}_{3/2}$ to $^4\text{I}_{15/2}$ transitions as a function of the grain sizes of NaYF₄:Yb-Er NPs; b) micro-area optical images of the as-fabricated films loaded with different sizes of upconversion NPs under irradiation at 980 nm: 1) NaYF₄:Yb-Er films; 2) NaYF₄:Yb-Er/W₁₈O₄₉ films.

size of ≈ 40 nm (Figure 4a). The as-synthesized $\text{NaYF}_4\text{:Yb-Er}@W_{18}\text{O}_{49}$ nanocomposite possesses a spherical structure that exposes numerous NWs on the surface, thus forming a “sea urchin-like” catalyst (Figure 4b). The diameters of the $\text{NaYF}_4\text{:Yb-Er}@W_{18}\text{O}_{49}$ heterostructures were around 1 μm . The TEM image shows that the NWs on the heterostructure surface are 400–600 nm in length and 10–30 nm in diameter. The TEM elemental mapping of an individual $\text{NaYF}_4\text{:Yb-Er}@W_{18}\text{O}_{49}$ heterostructure presents that the Na, Y, and F elements are mostly distributed in the center of the heterostructure, while the W and O elements are present throughout the whole profile, indicating the formation of the quasi-core/shell heterostructure (Figure 4c). The characterization results of the selected area electron diffraction (SAED) and XRD patterns unambiguously confirm that the as-synthesized heterostructures consisted of the cubic $\alpha\text{-NaYF}_4$ and the monoclinic $W_{18}\text{O}_{49}$ (Figure 4d,e). Notably, the $\text{NaYF}_4\text{:Yb-Er}@W_{18}\text{O}_{49}$ heterostructure still displayed an intense LSPR absorption band that overlaps with both the excitation and emission spectra of the $\text{NaYF}_4\text{:Yb-Er}$ NPs (Figure 4f). Taking this LSPR feature, the $\text{NaYF}_4\text{:Yb-Er}@$

$W_{18}\text{O}_{49}$ heterostructures also exhibited selectively enhanced upconversion emission, as deduced from the normalized emission spectra (Figure 4g). This suggests that the as-proposed NIR-plasmonic energy upconversion process occurs in the $\text{NaYF}_4\text{:Yb-Er}@W_{18}\text{O}_{49}$ heterostructure, which could offer a new and efficient way to enhance the catalytic H_2 evolution from BH_3NH_3 .

The catalytic activity of the as-synthesized $\text{NaYF}_4\text{:Yb-Er}@W_{18}\text{O}_{49}$ heterostructure was evaluated via hydrolysis of BH_3NH_3 under irradiation of 980 nm laser diode with a spot area of ≈ 0.5 cm^2 . As shown in Figure 5a, in the absence of catalysts, a very low H_2 evolution happened after 1 h of 980 nm irradiation (≈ 0.06 μmol), suggesting a slow hydrolysis process of BH_3NH_3 . When adding $W_{18}\text{O}_{49}$ NWs into the reaction solution without light irradiation, a slight increase in the H_2 evolution (≈ 0.12 μmol) could be observed (Figure S12, Supporting Information), demonstrating the poor catalytic activity of unexcited plasmonic $W_{18}\text{O}_{49}$ NWs. However, upon 980 nm irradiation, the H_2 evolution amount was substantially increased to ≈ 0.60 μmol after 1 h. The pure $\text{NaYF}_4\text{:Yb-Er}$ NPs

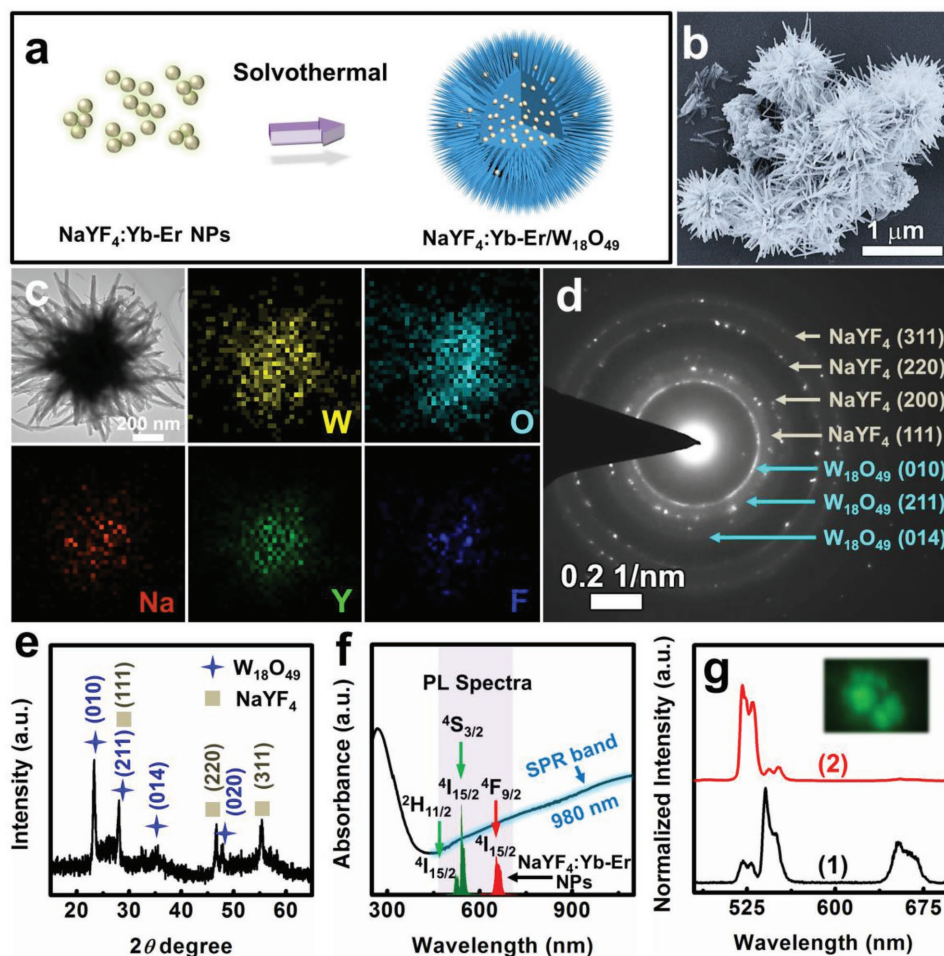


Figure 4. a) Schematic diagram of the synthesis route for the $\text{NaYF}_4\text{:Yb-Er}@W_{18}\text{O}_{49}$ quasi-core/shell heterostructure; b) SEM image of the $\text{NaYF}_4\text{:Yb-Er}@W_{18}\text{O}_{49}$ heterostructures; c) TEM image and the corresponding elemental mapping of an individual $\text{NaYF}_4\text{:Yb-Er}@W_{18}\text{O}_{49}$ heterostructure; d) SAED and e) XRD patterns of the $\text{NaYF}_4\text{:Yb-Er}@W_{18}\text{O}_{49}$ heterostructures; f) UV-vis-NIR absorption spectra of the $\text{NaYF}_4\text{:Yb-Er}@W_{18}\text{O}_{49}$ heterostructures and the upconversion emission spectra of the $\text{NaYF}_4\text{:Yb-Er}$ NPs; g) normalized upconversion emission spectra of 1) the $\text{NaYF}_4\text{:Yb-Er}$ NPs and 2) the $\text{NaYF}_4\text{:Yb-Er}@W_{18}\text{O}_{49}$ heterostructures. The inset provides the micro-area optical image of the 980 nm excited $\text{NaYF}_4\text{:Yb-Er}@W_{18}\text{O}_{49}$ heterostructures.

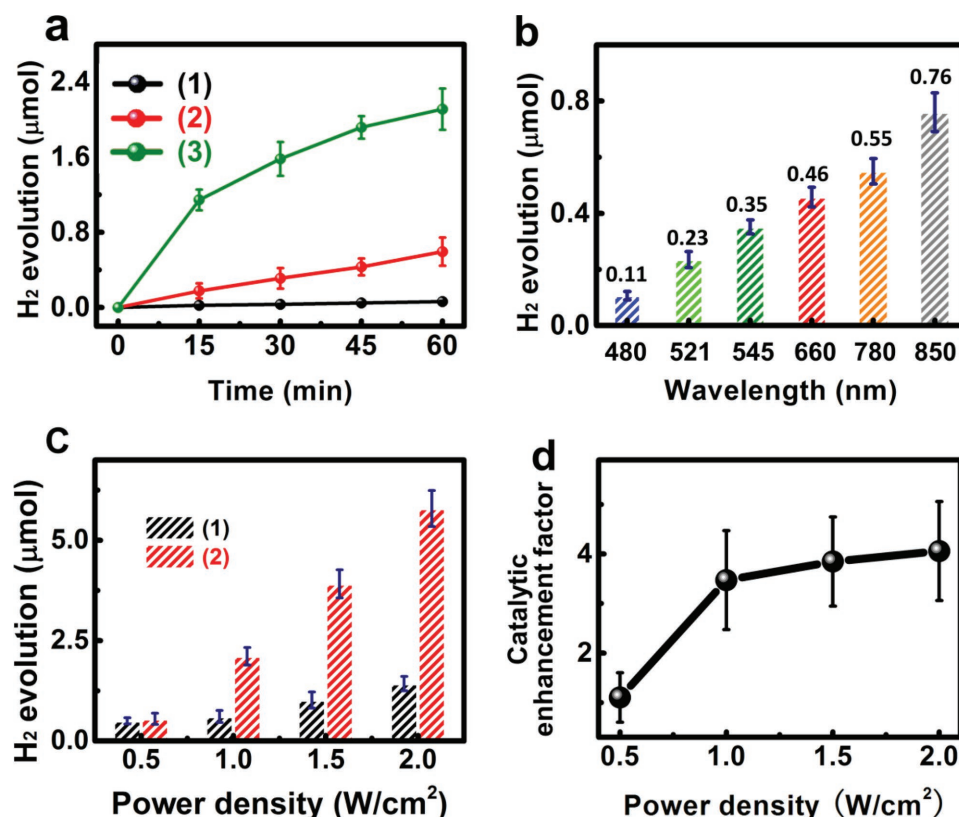


Figure 5. a) Plots of H₂ evolution amount versus reaction time of different catalysts in the BH₃NH₃ aqueous solution under irradiation at 980 nm: 1) Without any catalyst; 2) W₁₈O₄₉ NWs; 3) NaYF₄:Yb-Er@W₁₈O₄₉ heterostructures; b) H₂ evolution amount of the W₁₈O₄₉ NWs under irradiation with different incident light wavelengths for 1 h; c) power density-dependent H₂ evolution amount of 1) W₁₈O₄₉ NWs and 2) NaYF₄:Yb-Er@W₁₈O₄₉ heterostructures; d) plot of enhancement factor versus laser power density over NaYF₄:Yb-Er@W₁₈O₄₉ heterostructures.

showed a negligible H₂ generation (Figure S12, Supporting Information). These results revealed that the excited LSPR of W₁₈O₄₉ NWs could greatly boost the catalytic H₂ evolution due to the plasmonic transfer process of “hot electrons,” as outlined in previous publications.^[21,27] Importantly, the H₂ evolution amount of the NaYF₄:Yb-Er@W₁₈O₄₉ heterostructure can reach ≈2.11 μmol with the apparent quantum efficiency of ≈2.8% under 1 h irradiation of 980 nm (Equation (S22), Supporting Information). This H₂ evolution amount is about 3.5 times higher than the H₂ evolution of pure W₁₈O₄₉ NWs and even 35 times higher than the H₂ evolution of single BH₃NH₃ hydrolysis. Meanwhile, the apparent quantum efficiency is comparable to the corresponding values obtained in other visible-light photocatalysts.^[40–42] This implies that the upconversion NPs play a central role on the enhanced catalytic activity of the H₂ evolution. Namely, the upconversion emission of Ln³⁺-doped NaYF₄ NPs at a suitable wavelength region can improve the LSPR excitation of the W₁₈O₄₉ NWs and enhance the catalytic activity for H₂ evolution on the surface of W₁₈O₄₉ NWs. This hypothesis can be verified via wavelength-dependent H₂ evolution plots of W₁₈O₄₉ NWs. As shown in Figure 5b, the H₂ evolution amount of W₁₈O₄₉ NWs is directly correlated with the photon energy that can be absorbed by the W₁₈O₄₉ NWs to drive the LSPR effect.^[21,24,27,38] It is apparent that the LSPR band of W₁₈O₄₉ NWs overlapped with the green and red emissions of the NaYF₄:Yb-Er NPs. As a result of this, the enhanced catalytic activity of the NaYF₄@W₁₈O₄₉ heterostructures can be

attributed to the NIR-plasmonic energy upconversion induced by the LSPR effect of W₁₈O₄₉ NWs.

If this were true, the catalytic enhancement factor should be related to the excitation power density of the incident light.^[43,44] As shown in Figure 5c, the H₂ evolution amounts of both the W₁₈O₄₉ NWs and NaYF₄:Yb-Er@W₁₈O₄₉ heterostructures depended strongly on the power density of 980 nm laser diode. Furthermore, the enhancement factor gradually increased with the power density of incident light (Figure 5d). Therefore, it can be concluded that the light intensity illuminated on W₁₈O₄₉ dominated the enhanced catalytic activity. Besides, the NaYF₄@W₁₈O₄₉ heterostructure was also a reusable plasmonic catalyst (Figure S13, Supporting Information). Furthermore, the catalytic activity of NaYF₄:Yb-Er@W₁₈O₄₉ heterostructures for H₂ evolution increases with the size of NaYF₄:Yb-Er hetero-component (Figure S14, Supporting Information). Also note that a NaYF₄:Yb-Er/W₁₈O₄₉ film with the larger sizes of NaYF₄:Yb-Er NPs exhibited a higher intensity of upconversion luminescence, but a smaller enhancement factor. Thus, coupling plasmonic W₁₈O₄₉ NWs with the larger sizes of NaYF₄:Yb-Er NPs in their heterostructure could lead to a more efficient NIR-plasmonic energy upconversion to excite the LSPR of W₁₈O₄₉ NWs for catalytic H₂ evolution.

In summary, we have demonstrated the selective enhancement of upconversion luminescence behavior on the well-designed heterostructure film fabricated via self-assembly of NaYF₄:Yb-Er NPs onto the nonmetallic plasmonic layer of

W₁₈O₄₉ NWs grown on an FTO glass substrate. Investigations showed that the broad LSPR absorption band of W₁₈O₄₉ NWs overlapped with both the excitation and emission bands of NaYF₄:Yb-Er NPs, which could induce an NIR-plasmonic energy upconversion process, thus resulting in 9- to 112-fold enhancement of green emission on the NaYF₄:Yb-Er/W₁₈O₄₉ film as compared to the pure NaYF₄:Yb-Er NP film. By using this fascinating photophysical process, we also realized a promoted catalytic activity for H₂ evolution from BH₃NH₃ over the quasi-core/shell heterostructure of NaYF₄:Yb-Er NPs@W₁₈O₄₉ NWs under low-energy 980 nm excitation. The amount of H₂ evolution of the heterostructure was 35 times higher than that of BH₃NH₃ hydrolysis after irradiation with 980 nm for 1 h. Our study not only developed feasible and low-cost tactics to selectively enhance the upconversion luminescence of Ln³⁺-doped NaYF₄ NPs, but also offered a new class of NIR-responsive heterostructure catalysts that possess an efficient catalytic activity for H₂ evolution based on the NIR-plasmonic energy upconversion process.

Supporting Information

Supporting Information is available from the Wiley Online Library or from the author.

Acknowledgements

This work was supported by the National Natural Science Foundation of China (Grant Nos: 11474046, 51772041, 61775024, 11704058, and 21503034), the Natural Science Foundation of Liaoning Province (20170540190), the Program for Liaoning Innovation Team in University (LT2016011), the Program for Liaoning Excellent Talents in University (LNET) (Grant Nos. LR2015016 and LR2017004), the Program for Dalian Excellent Talents (Grant No. 2016RQ069), the Science and the Technique Foundation of Dalian (Grant Nos. 2017TD12 and 2015J12JH201), the Fundamental Research Funds for Central Universities, and the Foundation (Grant No. DUT16RC(3)111).

Conflict of Interest

The authors declare no conflict of interest.

Keywords

H₂ evolution, lanthanide ions, plasmonic semiconductors, upconversion luminescence

Received: May 14, 2018

Revised: June 3, 2018

Published online: July 3, 2018

- [1] S. Linic, P. Christopher, D. B. Ingram, *Nat. Mater.* **2011**, *10*, 911.
- [2] J. Wu, Z. Zhang, B. Liu, Y. Fang, L. Wang, B. Dong, *Sol. RRL*, **2018**, *2*, 1800039.
- [3] N. Zhang, C. Han, Y. J. Xu, J. J. F. Iv, D. Zhang, J. Codrington, S. K. Gray, Y. Sun, *Nat. Photonics* **2016**, *10*, 473.
- [4] D. M. Wu, A. García-Etxarri, A. Salleo, J. A. Dionne, *J. Phys. Chem. Lett.* **2014**, *5*, 4020.
- [5] C.-H. Cho, C. O. Aspetti, J. Park, R. Agarwal, *Nat. Photonics* **2013**, *7*, 285.
- [6] A. D. Johnson, F. Cheng, Y. Tsai, C.-K. Shih, *Nano Lett.* **2017**, *17*, 4317.
- [7] Z. Yin, H. Li, W. Xu, S. Cui, D. Zhou, X. Chen, Y. Zhu, G. Qin, H. Song, *Adv. Mater.* **2016**, *28*, 2518.

- [8] M. Saboktakin, X. Ye, U. K. Chettiar, N. Engheta, C. B. Murray, C. R. Kagan, *ACS Nano* **2013**, *7*, 7186.
- [9] Z. Wang, C. Wang, Q. Han, G. Wang, M. Zhang, J. Zhang, W. Gao, H. Zheng, *Mater. Res. Bull.* **2017**, *88*, 182.
- [10] Z. Xu, M. Quintanilla, F. Vetrone, A. O. Govorov, M. Chaker, D. Ma, *Adv. Funct. Mater.* **2015**, *25*, 2950.
- [11] Y. Tang, W. Di, X. Zhai, R. Yang, W. Qin, *ACS Catal.* **2013**, *3*, 405.
- [12] D. Lu, S. K. Cho, S. Ahn, L. Brun, C. J. Summers, W. Park, *ACS Nano* **2014**, *8*, 7780.
- [13] W. Zhang, F. Ding, S. Y. Chou, *Adv. Mater.* **2012**, *24*, OP236.
- [14] J. A. Schuller, E. S. Barnard, W. Cai, Y. C. Jun, J. S. White, M. L. Brongersma, *Nat. Mater.* **2010**, *9*, 193.
- [15] A. Zaleska-Medynska, M. Marchelek, M. Diak, E. Grabowska, *Adv. Colloid Interface Sci.* **2016**, *229*, 80.
- [16] X. Liu, M. T. Swihart, *Chem. Soc. Rev.* **2014**, *43*, 3908.
- [17] S. Zhou, X. Pi, Z. Ni, Y. Ding, Y. Jiang, C. Jin, C. Delerue, D. Yang, T. Nozaki, *ACS Nano* **2015**, *9*, 378.
- [18] J. M. Luther, P. K. Jain, T. Ewers, A. P. Alivisatos, *Nat. Mater.* **2011**, *10*, 361.
- [19] D. Dorfs, T. Härtling, K. Miszta, N. C. Bigall, M. R. Kim, A. Genovese, A. Falqui, M. Povia, L. Manna, *J. Am. Chem. Soc.* **2011**, *133*, 11175.
- [20] M. Kanehara, H. Koike, T. Yoshinaga, T. Teranishi, *J. Am. Chem. Soc.* **2009**, *131*, 17736.
- [21] H. Cheng, T. Kamegawa, K. Mori, P. H. Yamashita, *Angew. Chem., Int. Ed.* **2014**, *53*, 2910.
- [22] D. Zhou, D. Liu, W. Xu, Z. Yin, X. Chen, P. Zhou, S. Cui, Z. Chen, H. Song, *ACS Nano* **2016**, *10*, 5169.
- [23] Y. Xie, L. Carbone, C. Nobile, V. Grillo, S. D'Agostino, S. F. Della, C. Giannini, D. Altamura, C. Oelsner, C. Krysch, *ACS Nano* **2013**, *7*, 7352.
- [24] Z. Zhang, X. Jiang, B. Liu, L. Guo, N. Lu, L. Wang, J. Huang, K. Liu, B. Dong, *Adv. Mater.* **2018**, *30*, 1705221.
- [25] Z. Zhang, J. Huang, Y. Fang, M. Zhang, K. Liu, B. Dong, *Adv. Mater.* **2017**, *29*, 1606688.
- [26] J. Yan, T. Wang, G. Wu, W. Dai, N. Guan, L. Li, J. Gong, *Adv. Mater.* **2015**, *27*, 1580.
- [27] Z. Lou, Q. Gu, L. Xu, Y. Liao, C. Xue, *Chemistry* **2015**, *10*, 1291.
- [28] K. Ikeda, K. Takahashi, T. Masuda, H. Kobori, M. Kanehara, T. Teranishi, K. Uosaki, *J. Phys. Chem. C* **2012**, *116*, 20806.
- [29] S. Gao, K. Ueno, H. Misawa, *Acc. Chem. Res.* **2011**, *44*, 251.
- [30] W. Xu, Y. Zhu, X. Chen, J. Wang, L. Tao, S. Xu, T. Liu, H. Song, *Nano Res.* **2013**, *6*, 795.
- [31] Q. Sun, H. Mundoor, J. Ribot, V. Singh, I. Smalyukh, P. Nagpal, *Nano Lett.* **2014**, *14*, 101.
- [32] X. Liu, D. Y. Lei, *Sci. Rep.* **2015**, *5*, 15235.
- [33] P. Bharadwaj, L. Novotny, *Opt. Express* **2007**, *15*, 14266.
- [34] X. Chen, Y. Chen, M. Yan, M. Qiu, *ACS Nano* **2012**, *6*, 2550.
- [35] S. Fischer, N. D. Bronstein, J. K. Swabeck, E. M. Chan, A. P. Alivisatos, *Nano Lett.* **2016**, *16*, 7241.
- [36] B. Dong, B. Cao, Y. He, L. Zhuang, Z. Li, Z. Feng, *Adv. Mater.* **2012**, *24*, 1987.
- [37] B. Dong, B. Cao, Z. Feng, X. Wang, Y. He, *Sens. Actuators, B* **2012**, *165*, 34.
- [38] K. Fuku, R. Hayashi, S. Takakura, T. Kamegawa, K. Mori, H. Yamashita, *Angew. Chem.* **2013**, *52*, 7446.
- [39] Q. Gu, Z. Gao, C. Xue, *Small* **2016**, *12*, 3543.
- [40] Y. P. Yuan, L. S. Yin, S. W. Cao, G. S. Xu, C. H. Li, C. Xue, *Appl. Catal., B* **2015**, *168–169*, 572.
- [41] Z. Zhang, Y. Huang, K. Liu, L. Guo, Q. Yuan, B. Dong, *Adv. Mater.* **2015**, *27*, 5906.
- [42] K. Awazu, M. Fujimaki, C. Rockstuhl, J. Tominaga, H. Murakami, Y. Ohki, N. Yoshida, T. Watanabe, *J. Am. Chem. Soc.* **2008**, *130*, 1676.
- [43] B. Wu, D. Liu, S. Mubeen, T. T. Chuong, M. Moskovits, G. D. Stucky, *J. Am. Chem. Soc.* **2016**, *138*, 1114.
- [44] W. Hou, S. B. Cronin, *Adv. Funct. Mater.* **2013**, *23*, 1612.